

# Supplementary Information

for

## Identification and tunable optical coherent control of transition-metal spins in silicon carbide

by

Tom Bosma \*, Gerrit J. J. Lof \*, Carmem M. Gilardoni, Olger V. Zwiernicki, Freddie Hendriks, Björn Magnusson, Alexandre Ellison, Andreas Gällström, Ivan G. Ivanov, N. T. Son, Remco W. A. Havenith, and Caspar H. van der Wal

### TABLE OF CONTENTS

References	2
1. Single-laser spectroscopy	3
2. Additional two-laser spectroscopy for Mo in 6H-SiC	5
3. Two-laser spectroscopy for Mo in 4H-SiC	9
4. Franck-Condon principle with respect to spin	12
5. V-scheme dip	14
6. Modeling of coherent population trapping	17
7. Anisotropic g-factor in the effective spin-Hamiltonian	19

---

## REFERENCES FOR THE SUPPLEMENTARY INFORMATION

\* These authors contributed equally to this work.

1. Fox, M. *Optical properties of solids* (2nd edition). Oxford master series in condensed matter physics (Oxford University Press, Oxford, 2010).
2. Fleischhauer, M., Imamoglu, A., & Marangos, J. P. Electromagnetically induced transparency: Optics in coherent media. *Rev. Mod. Phys.* **77**, 633–673 (2005).
3. Ivády, V., Somogyi, B., Zólyomi, V., Gällström, A., Son, N. T., Janzén, E., & Gali, A. Transition metal defects in cubic and hexagonal polytypes of SiC: Site selection, magnetic and optical properties from AB INITIO calculations. *Mat. Sci. Forum* **717**, 205–210 (2012).
4. Baur, J., Kunzer, M., & Schneider, J. Transition metals in SiC polytypes, as studied by magnetic resonance techniques. *Phys. Status Solidi A* **162**, 153–172 (1997).
5. Abragam, A. & Bleaney, B. *Electron paramagnetic resonance of transition ions*. International series of monographs on physics (Clarendon Press, Oxford, 1970).
6. Chibotaru, L. F., Hendrickx, M. F. A., Clima, S., Larionova, J., & Ceulemans, A. Magnetic anisotropy of  $[\text{Mo}(\text{CN})_7]^{4-}$  anions and fragments of cyano-bridged magnetic networks. *The Journal of Physical Chemistry A* **109**, 7251–7257 (2005).
7. Kunzer, M., Müller, H. D., & Kaufmann, U. Magnetic circular dichroism and site-selective optically detected magnetic resonance of the deep amphoteric vanadium impurity in 6H-SiC. *Physical Review B* **48**, 10846–10854 (1993).
8. Dietz, R., Kamimura, H., Sturge, M., & Yariv, A. Electronic structure of copper impurities in ZnO. *Physical Review* **132**, 1559–1569 (1963).

## 1. SINGLE-LASER SPECTROSCOPY

Figure S1 shows the photoluminescence (PL) emission spectrum of the 4H-SiC sample at 5 and 20 K, characterized using a 514.5 nm excitation laser. The Mo zero-phonon line (ZPL) at 1.1521 eV is marked by a dashed box and shown enlarged in the inset. The broader peaks at lower energies are phonon replicas of the ZPL. There is almost no dependence on temperature for both the ZPL and the phonon replicas.

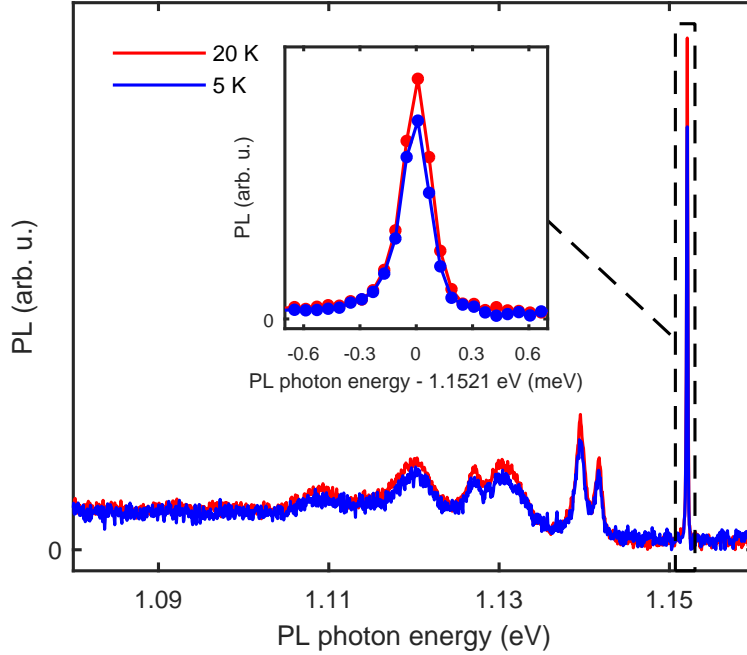


FIG. S1: **Temperature dependence of Mo PL spectrum in 4H-SiC.** PL from excitation with a 514.5 nm laser, for 5 and 20 K sample temperatures. The dashed box marks the ZPL at 1.1521 eV. The inset gives a magnified view of the ZPL. The broader peaks at lower photon energies are phonon replicas of the ZPL.

Figures S2a,b show results of PLE measurements of the ZPL for Mo in 4H-SiC at 1.1521 eV and 6H-SiC at 1.1057 eV, and the temperature dependence of these PLE signals. When the temperature is decreased, the width of the ZPL stays roughly the same, but its height drops significantly. Combined with the near-independence on temperature of the emission spectrum in Fig. S1, this is an indication for optical spin pumping for Mo-impurity states at lower temperatures, where a single resonant laser pumps then the system into long-lived off-resonant spin states.

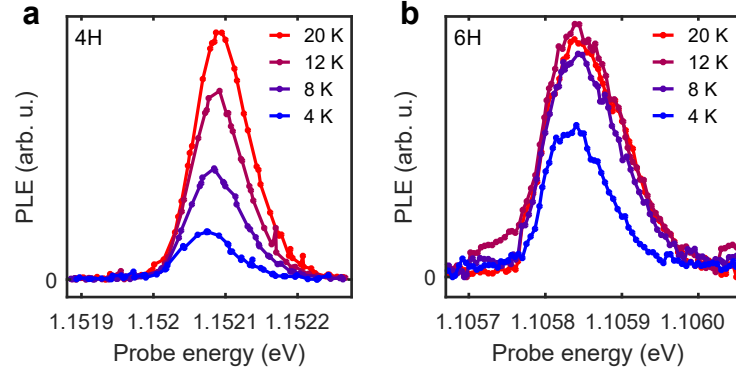


FIG. S2: **Temperature dependence of the PLE signals from the Mo ZPL in 4H-SiC and 6H-SiC.** PLE signals from scanning a single CW narrow-linewidth laser across the ZPL photon-energy range. The temperature was varied between 4 and 20 K. The ZPL for Mo in (a) 4H-SiC is at 1.1521 eV, and for Mo in (b) 6H-SiC at 1.1057 eV.

## 2. ADDITIONAL TWO-LASER SPECTROSCOPY FOR Mo IN 6H-SiC

*a. Angle dependence.* In addition to Fig. 2b,c in the main text, we also measured the magnetic field dependence of the spin related emission signatures at intermediate angles  $\phi$ . Figure S3 shows this dependence for  $\phi = 37^\circ$ ,  $57^\circ$  and  $81^\circ$ . The spectroscopic position of emission lines  $L_n$  show a linear dependence on magnetic field, with slopes  $\Theta_{L_n}$  (in Hertz per Tesla) that decrease as  $\phi$  increases. The effective g-factors in Fig. 4 are acquired from the emission lines by relating their slopes to the Zeeman splittings in the ground and excited state. Using the four pumping schemes depicted in Fig. 3 in the main text, we derive

$$\Theta_{L1} = \frac{\mu_B}{h} g_g \quad (5)$$

$$\Theta_{L2} = \frac{\mu_B}{h} |g_e - g_g| \quad (6)$$

$$\Theta_{L3} = \frac{\mu_B}{h} g_e \quad (7)$$

$$\Theta_{L4} = \frac{\mu_B}{h} (g_e + g_g) \quad (8)$$

where  $h$  is Planck's constant,  $\mu_B$  the Bohr magneton and  $g_{g(e)}$  the ground (excited) state g-factor.

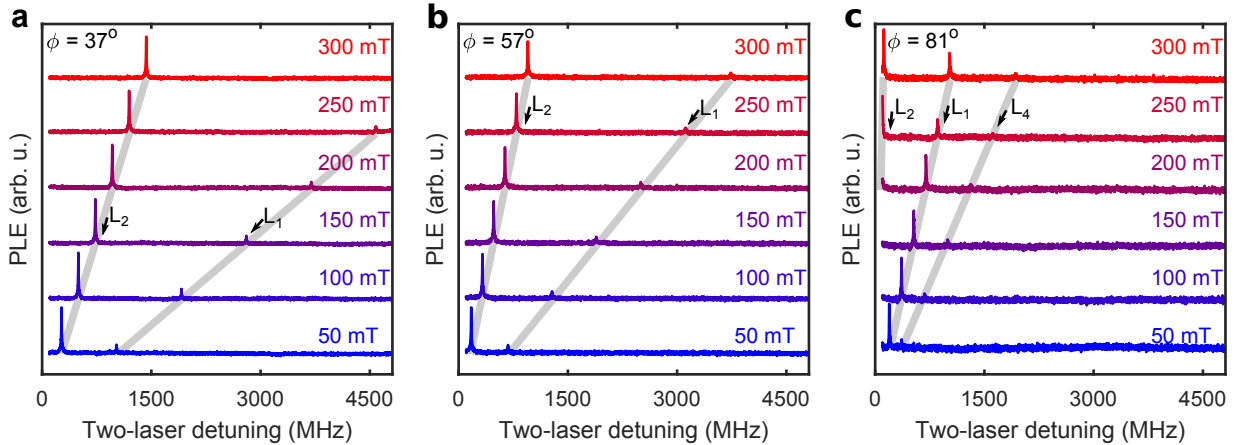


FIG. S3: **Magneto-spectroscopy of two-laser spin signatures in PLE from Mo in 6H-SiC.** Magnetic field dependence of the PLE signal as a function of two-laser detuning, for angles  $\phi$  between the magnetic field and c-axis set to  $\phi = 37^\circ$  (a),  $\phi = 57^\circ$  (b) and  $\phi = 81^\circ$  (c). Results for the temperature at 4 K. The labeling of the emission lines ( $L_1 - L_4$ ) is consistent with Fig. 2. The data are offset vertically for clarity.

*b. Temperature and photon-energy dependence.* We also measured the dependence of the two-laser PLE signal on temperature, see Fig. S4a. The PLE features disappear above 8 K in a much broader PLE background that starts to emit because of more rapid thermal spin mixing in the ground state. Other Mo systems in the ensemble for which the two-laser resonance condition is not met then also start emitting due to single-laser excitation (see also Fig. S2), since the optical pumping into an off-resonant state becomes shorter lived. Notably, the linewidths of the peaks in Fig. S4a do not change in the range 2 K to 8 K, indicating that the temperature does not affect the optical lifetime in this range. Above 8 K the temperature was a bit unstable during the measurements, which causes the drifting in the single-laser PLE contribution to this signal. Interestingly, the dip ( $L_3$ ) is most pronounced at 6 K, since there are several competing processes responsible for this dip (see section 5).

Additionally, we measured how the two-laser PLE occurred throughout the inhomogeneously broadened ensemble, by varying the photon energy of the control laser and sweeping the two-laser detuning for each case (Fig. S4b). For all photon energies the peaks are at the same position, indicating that all Mo atoms in the ensemble behave similarly. At 1.10561 eV the control laser is too far detuned from the ZPL to yield any two-laser PLE signal.

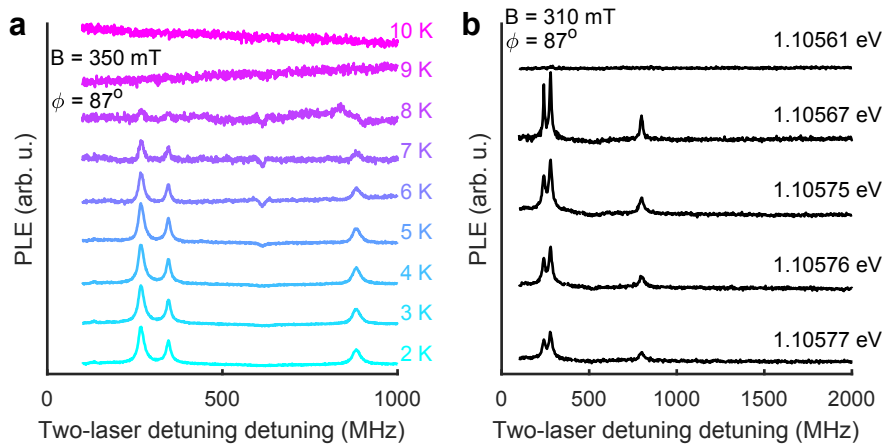


FIG. S4: **Temperature and photon-energy dependence of two-laser emission features in 6H-SiC.** Temperature (a) and laser photon-energy (b) dependence of the PLE signal as a function of two-laser detuning. Results are offset vertically for clarity.

*c. Two-laser spectroscopy for the 5-21 GHz detuning range.* In order to check for a possible presence of spin-related emission features at detunings larger than 5 GHz (checking for a possible zero-field splitting), we modified the setup such that we could control two-laser detunings up to 21 GHz. The electro-optical phase modulator (EOM) we used for generating the detuned laser field could generate first-order sidebands up to 7 GHz. In order to check for two-laser spectroscopy emission features at larger detunings, we removed the Fabry-Pérot (FP) resonator that had the role of filtering out a single sideband. Now, all sidebands (on the same optical axis) were focused onto the sample with 2 mW total laser power. Apart from the re-pump beam, no additional laser was focused onto the sample in this experiment. In this way, the Mo defects could interact with several combinations of sidebands. Figure S5a shows the spectral content of this beam (here characterized by still using the FP resonator). The first and second order sidebands at negative and positive detuning take a significant portion of the total optical power. Hence, pairs of sidebands spaced by single, double or triple frequency intervals (EOM frequency  $f_{\text{EOM}}$ ) now perform two-laser spectroscopy on the Mo defects. The relevant sideband spacings are indicated in Fig. S5a.

Figure S5b presents results of these measurements, showing various peaks that we identified and label as  $L_{n,m}$ . Here  $n$  is identifying the peak as a line  $L_n$  as in the main text, while the label  $m$  identifies it as a spectroscopic response for two-laser detuning at  $m \cdot f_{\text{EOM}}$  (that is,  $m = 1$  is for first-order EOM sideband spacing, *etc.*). Note that second-order manifestations of the known peaks  $L_1$ - $L_4$  (from double sideband spacings, labeled as  $L_{n,2}$ ) are now visible at  $\frac{1}{2}f_{\text{EOM}}$ , and third-order response of the known  $L_1$ - $L_4$  occurs at  $\frac{1}{3}f_{\text{EOM}}$  (but for preserving clarity these have not been labeled in Fig. S5b).

Figure S5c depicts a continuation of this experiment with  $f_{\text{EOM}}$  up to 7 GHz with the same resolution as Fig. S5b. No new peaks are observed. Considering that third-order peaks were clearly visible before, we conclude that no additional two-laser emission features exist up to 21 GHz.

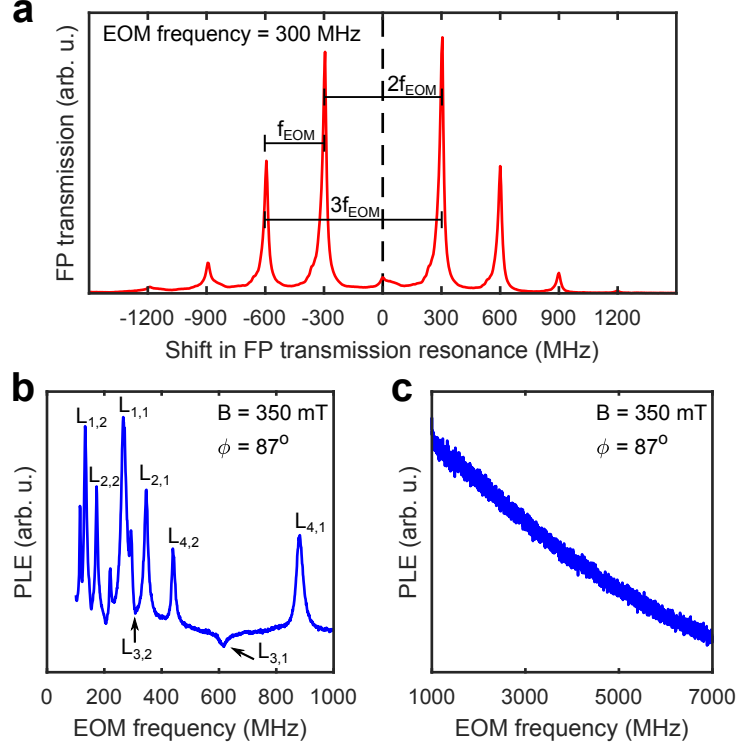


FIG. S5: **Two-laser spin signatures of Mo in 6H-SiC at large detuning.** **a**, Transmission scan of the Fabry-Pérot resonator, characterizing which optical frequencies are present in the beam after passing through the electro-optical modulator (EOM). The first-order sidebands at  $\pm 300$  MHz have the highest intensity, whereas the fundamental laser frequency is suppressed (but not fully removed) by the EOM. Relevant sideband spacings are indicated. **b**, Spin signatures at low two-laser detuning. PLE is increased when two sidebands are appropriately detuned from each other. Emission features similar to those in Fig. 2c of the main text are visible, and labeled  $L_{n,m}$  (see main text of this section). **c**, The PLE signal from two-laser spectroscopy at larger detuning. No peaked features from single, double or triple sideband spacings are visible.

### 3. TWO-LASER SPECTROSCOPY FOR Mo IN 4H-SiC

We also studied the spin-related fine structure of Mo defects in 4H-SiC. Our 4H-SiC sample suffered from large background absorption, which drastically lowered the signal-to-noise ratio. We relate this absorption to a larger impurity content (of unknown character, but giving broad-band absorption) in our 4H-SiC material as compared to our 6H-SiC material. Therefore, the lasers were incident on a corner of the sample, so as to minimize the decay of the emitted PL. We present the results in gray-scale plots in Fig. S6 for optimized contrast. The figure shows the magnetic field and two-laser detuning dependence of the PLE.

Analogous to Fig. 2 for 6H-SiC in the main text, the spectroscopic position features appear as straight lines that emerge from zero detuning, indicating the absence of a zero-field splitting. When the magnetic field is nearly perpendicular to the c-axis (Fig. S6c), four lines are visible. This is consistent with an  $S = 1/2$  ground and excited state.

The data from Fig. S6c was measured at 10 K, whereas Fig. S6a,b was at 4.2 K. At 10 K, all emission lines become dips, while for 6H-SiC only the V system shows a dip. The temperature dependence of  $L_3$  and  $L_1$  is shown in Fig. S7 for the same configuration as in Fig. S6c ( $\phi = 83^\circ$ ). At low temperatures  $L_1$  shows a peak and  $L_3$  shows a dip. Upon increasing the temperature, both features become dips. This phenomenon was only observed for Mo in 4H-SiC, it could not be seen in 6H-SiC. We therefore conclude that this probably arises from effects where Mo absorption and emission is influenced by the large background absorption in the 4H-SiC material.

The labels in Fig. S6 are assigned based on the sum rules from equation (2) and (3) (main text), which indeed also hold for the observed emission lines observed here. Like in the main text,  $L_1$  through  $L_4$  indicate  $\Lambda$ ,  $\Pi$ , V and X two-laser pumping schemes, respectively. The  $L_1$  and  $L_3$  labels are interchangeable in Fig. S6c when only considering the sum rules. However, the fact that the left feature in Fig. S7 shows a dip for all temperatures means that it should be related to a V scheme. Thus, the current assignment of the labels with corresponding pumping schemes is justified. Using equations 5 through 8 (Suppl. Inf.), the effective g-factors can be determined. Fitting these to equation (4) gives the values for  $g_{\parallel}$  and  $g_{\perp}$  reported in the main text.

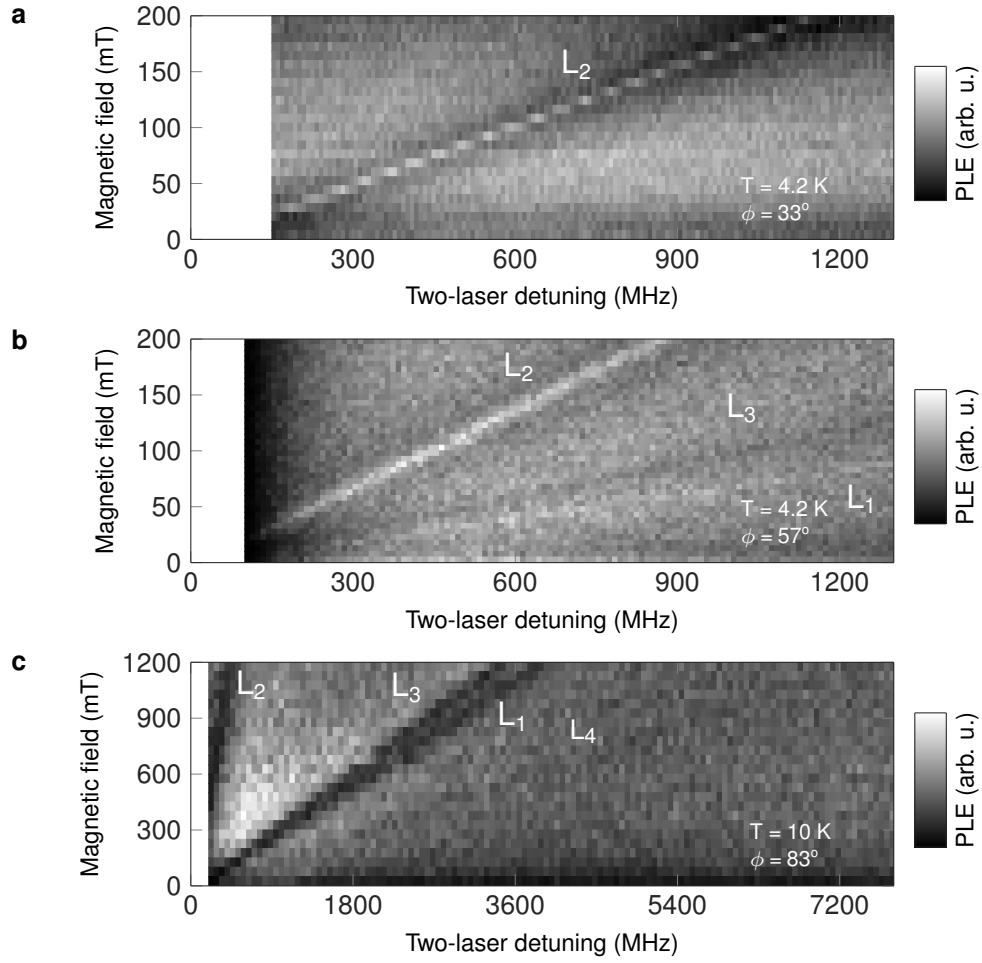


FIG. S6: **Two-laser spin signatures of Mo in 4H-SiC.** PLE signal as a function of two-laser detuning and magnetic field strength, for various angles  $\phi$  between the magnetic field and c-axis. **a**, Measurement at 4.2 K, with  $\phi = 33^\circ$ . A single emission line (peak) is visible, labeled  $L_2$ . **b**, Measurement at 4.2 K, with  $\phi = 57^\circ$ . Three emission lines are visible, labeled  $L_1$ ,  $L_2$  (peaks), and  $L_3$  (dip). **c**, Measurement at 10 K, with  $\phi = 83^\circ$ . Four emission lines are visible, labeled  $L_1$  through  $L_4$  (all dips). Note that the measurement range of **c** is six times as large as **a** and **b**, but the plot aspect ratio is the same. The labeling is consistent with the main text. A gray-scale plot has been used for optimal contrast.

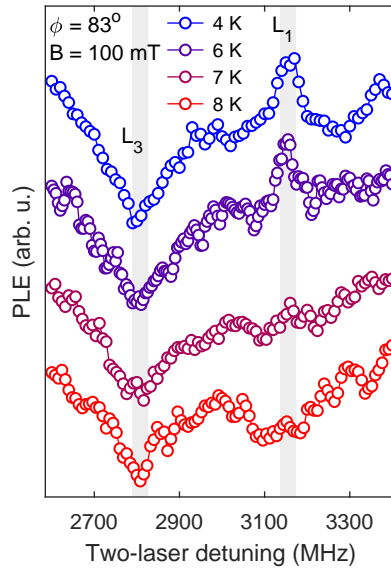


FIG. S7: **Temperature dependence of PLE spin signatures from Mo in 4H-SiC.** PLE signal as a function of two-laser detuning and temperature with magnetic field at  $\phi = 83^\circ$  from the sample c-axis at 100 mT. As the temperature increases, the signal from  $L_1$  changes from a peak to a broad dip, while  $L_3$  remains a dip. The labeling is consistent with the main text.

#### 4. FRANCK-CONDON PRINCIPLE WITH RESPECT TO SPIN

The amplitude of the two-laser emission signatures is determined by the strength of the underlying optical transitions. For a transition  $|g_i\rangle\text{-}|e_j\rangle$ , this strength is determined by the spin overlap  $\langle g_i|e_j\rangle$ , according to the Franck-Condon principle with respect to spin<sup>1</sup>. The quantum states of the spin in the electronic ground and excited state can be described using effective spin Hamiltonian

$$H_{g(e)} = \mu_B \mathbf{B} \cdot \mathbf{g}_{g(e)} \cdot \tilde{\mathbf{S}} \quad (9)$$

with  $\mu_B$  the Bohr magneton,  $\mathbf{B}$  the applied magnetic field vector,  $\tilde{\mathbf{S}}$  the effective spin vector, and where the ground (excited) state g-parameter is a tensor  $\mathbf{g}_{g(e)}$ . Using Cartesian coordinates this can be written as

$$\mathbf{g}_{g(e)} = \begin{pmatrix} g_{\perp}^{g(e)} & 0 & 0 \\ 0 & g_{\perp}^{g(e)} & 0 \\ 0 & 0 & g_{\parallel}^{g(e)} \end{pmatrix} \quad (10)$$

Here the  $z$ -axis is parallel to the SiC  $c$ -axis, and the  $x$  and  $y$ -axes lay in the plane perpendicular to the  $c$ -axis. Due to the symmetry of the defect, the magnetic field  $\mathbf{B}$  can be written as

$$\mathbf{B} = \begin{pmatrix} 0 \\ B \sin \phi \\ B \cos \phi \end{pmatrix} \quad (11)$$

where  $B$  indicates the magnitude of the magnetic field. The resulting Hamiltonian  $H_{g(e)}$  may be found by substituting  $\mathbf{B}$  and  $\mathbf{g}_{g(e)}$  into equation (9), and considering that  $S = 1/2$ . The basis of  $H_{g(e)}$  can be found from the eigenvectors.

For the ground state  $g_{\perp}^g$  is zero, thus the bases of  $H_g$  and  $S_z$  coincide, independent of  $\phi$ . Therefore, there is no mixing of spins in the ground state. However, in the excited state  $g_{\perp}^e$  is nonzero, causing its eigenbasis to rotate if a magnetic field is applied non-parallel to the  $c$ -axis. The new eigenbasis is a linear combination of eigenstates of  $S_x$ ,  $S_y$  and  $S_z$ , such that there will be mixing for spins in the excited state for any nonzero angle  $\phi$ .

We calculate the spin overlap for the  $|g_i\rangle\text{-}|e_j\rangle$  transition from the inner product of two basis states  $|g_i\rangle$  and  $|e_j\rangle$ . The strength of a two-laser pumping scheme is then the product of the strength of both transitions. For example, the strength of the  $\Lambda$  scheme from Fig. 3a

equals the inner product  $\langle g_1 | e_2 \rangle$  multiplied by  $\langle g_2 | e_2 \rangle$ . The resulting strengths for all four pumping schemes are depicted in Fig. S8.

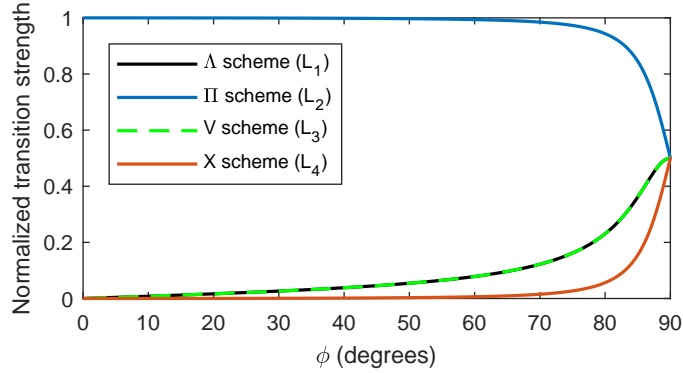


FIG. S8: **Two-laser pumping scheme transition strengths.** For each scheme the product of the spin overlaps from both underlying transitions is shown. The strength of the II scheme is near unity for large angles and never vanishes. The strengths of the  $\Lambda$  and V schemes are equal, they vanish at  $\phi = 0^\circ$ . The X scheme strength vanishes more rapidly than any other scheme for angles  $\phi$  close to  $0^\circ$ .

We now compare these transition strengths to the data in Fig. 2b,c and Fig. S3 and S6. It is clear that the II scheme is the strongest pumping scheme for all angles  $\phi \neq 90^\circ$ . This explains the large relative amplitude of  $L_2$  in our measurements. The  $\Lambda$  and V scheme transition strengths are equal, starting from zero for  $\phi = 0^\circ$  and increasing as  $\phi$  approaches  $90^\circ$ . For the  $\Lambda$  scheme, this is consistent with the increasing relative amplitude of  $L_1$ . For  $\phi$  close to  $90^\circ$  the amplitude of  $L_1$  is even larger than for  $L_2$ . The reason for this is that a  $\Lambda$  scheme is emitting more effectively than a II scheme. The V scheme is harder to observe in the background emission, such that  $L_3$  is only visible for  $\phi$  close to  $90^\circ$ . Finally, the transition strength of the X scheme is only significant for  $\phi$  close to  $90^\circ$ , which is why we have not been able to observe  $L_4$  below  $81^\circ$  in 6H-SiC.

## 5. V-SCHEME DIP

Understanding the observation of a dip for the V pumping scheme in a four-level system (Fig. 2c in the main text) is less trivial than for the observation of peaks from the other three pumping schemes. The latter can be readily understood from the fact that for proper two-laser detuning values both ground states are addressed simultaneously, such that there is no optical pumping into dark states. In this section we will investigate how a dip feature can occur in the PLE signals. Our modeling will be based on solving a master equation in Lindblad form with a density matrix in rotating wave approximation for a four-level system with two near-resonant lasers<sup>2</sup>.

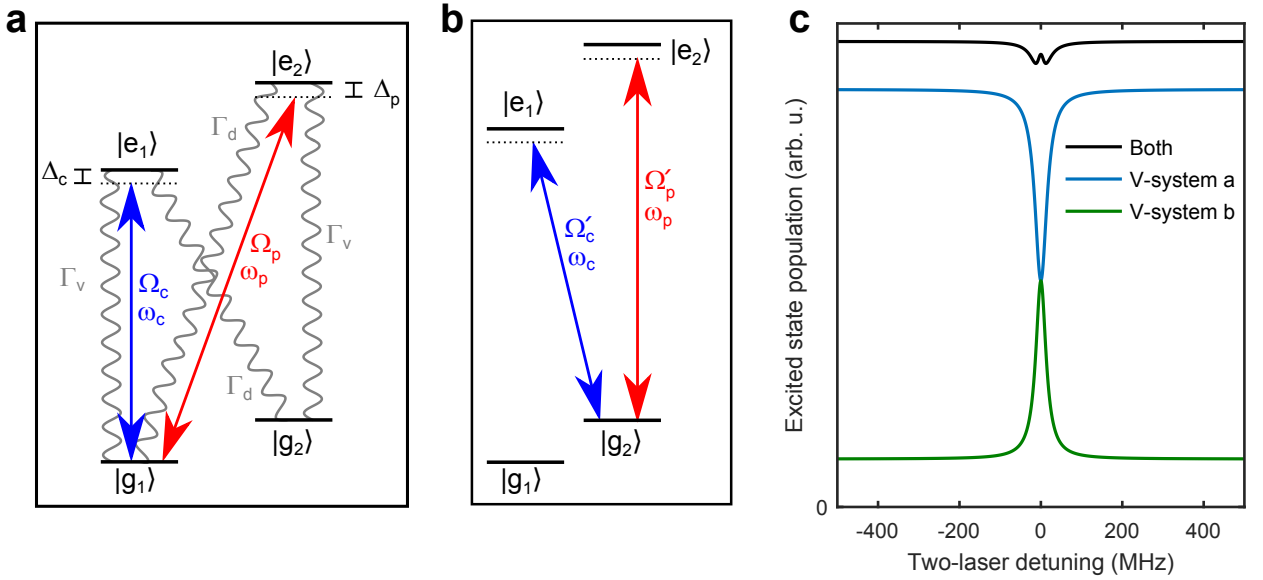


FIG. S9: **Four-level V-scheme model.** **a**, V pumping scheme in a four level system. Here  $\Omega$  is the Rabi frequency for the control and probe lasers, and  $\omega$  their (angular) frequency.  $\Gamma_v$  and  $\Gamma_d$  are the decay rates for vertical and diagonal decay, respectively.  $\Delta$  represents the detuning from resonance of the control and probe beam. **b**, V-scheme simultaneously resonant (with the scheme in panel **a**) for another part of the inhomogeneously broadened ensemble. Probe and control Rabi frequencies  $\Omega'$  differ from **a**, since both lasers drive other transitions with different dipole strengths. **c**, Total population in the excited-state levels ( $|e_1\rangle$  and  $|e_2\rangle$ ) for both schemes separately (blue and green) as well as their sum (black).

TABLE S1: **Parameter choices for V-scheme model**

parameter	value (Hz)	parameter	value (Hz)
$\Gamma_v$	$0.9 \cdot 10^7$	$\gamma_{g1}$	0
$\Gamma_d$	$0.1 \cdot 10^7$	$\gamma_{g2}$	$5 \cdot 10^6$
$\Gamma_g$	$1 \cdot 10^4$	$\gamma_{g3}$	$5 \cdot 10^6$
$\Gamma_e$	$1 \cdot 10^4$	$\gamma_{g4}$	$5 \cdot 10^6$
$\Delta_c$	0	$\Omega_c$	$\sqrt{.9} \cdot 10^7$
$\Delta_p$	$\in [-500, 500] \cdot 10^6$	$\Omega_p$	$\sqrt{.1} \cdot 10^7$

Consider the four-level system depicted in Fig. S9a. A control laser is near-resonant with the  $|g_1\rangle$ - $|e_1\rangle$  (vertical) transition and a probe laser near-resonant with  $|g_1\rangle$ - $|e_2\rangle$  (diagonal) transition. Here the two-laser detuning is defined as  $\delta = \Delta_p - \Delta_c$ , *i.e.* the difference between the detunings  $\Delta$  of both lasers from their respective near-resonant transitions, such that the emission feature appears at zero two-laser detuning. The decay rates from the excited states are  $\Gamma_v$  and  $\Gamma_d$  for vertical and diagonal transitions, respectively. They are quadratically proportional to the spin-state overlap  $\langle g_i | e_j \rangle$

$$\Gamma_v \propto |\langle g_1 | e_1 \rangle|^2, \quad (12)$$

$$\Gamma_d \propto |\langle g_1 | e_2 \rangle|^2. \quad (13)$$

These rates are unequal, since the spin-state overlap for diagonal transitions is generally smaller than for vertical transitions (see previous section). The decay rates  $\Gamma_e$  between excited-state levels and  $\Gamma_g$  ground-state levels are assumed very small compared to the decay rates from the excited-state levels. The decay rates from ground-state levels towards the excited-state levels are set to zero. Dephasing rates are taken relative to the  $|g_1\rangle$  state ( $\gamma_{g1} = 0$ ). The choices for parameters are listed in table S1. The Rabi frequencies  $\Omega_c$  and  $\Omega_p$  of the driven transitions are linearly proportional to the spin-state overlap

$$\Omega_c \propto |\langle g_1 | e_1 \rangle|, \quad (14)$$

$$\Omega_p \propto |\langle g_1 | e_2 \rangle|. \quad (15)$$

Additionally, we have to consider a secondary V-scheme (Fig. S9b) resonant with another part of the inhomogeneously broadened ensemble. The control and probe laser are swapped,

as the former now addresses a diagonal transition, while the latter addresses a vertical one. The new Rabi frequency is taken to be  $\Omega'_c = \sqrt{\frac{\Gamma_d}{\Gamma_v}}\Omega_c$  for the control beam, which is now driving a diagonal transition (with reduced strength). The probe beam is driving a vertical transition (with increased strength), and its Rabi frequency is  $\Omega'_p = \sqrt{\frac{\Gamma_v}{\Gamma_d}}\Omega_p$ .

Considering both V-schemes, we calculate the total population in both excited-state levels as it reflects the amount of photoluminescence resulting from decay back to the ground states. The two-laser detuning dependence of the excited-state population is shown in Fig. S9c. The black curve considers both schemes simultaneously, which represents the situation in our measurements. Here the dip indeed appears, although both separate schemes (a and b) display a dip and peak (respectively). The competition between both schemes limits the depth of the observed dip, which explains our observation of shallow dips in contrast to sharp peaks in Fig. 2c in the main text.

Interestingly, the black curve displays a peak within the dip, which might seem like a CPT feature. However, this feature is not visible in either curve from the two separate pumping schemes. This peak appears because the peak from the second V-scheme (green) is slightly sharper than the dip from the first one (blue). The peak might still be caused by CPT, as the blunting of the dip relative to the peak can be caused by a long dephasing time of the ground state.

Key to understanding the appearance of a dip in the total photoluminescence emission is the difference in decay rates, vertical decay being favored over diagonal decay. Consider the pumping scheme from Fig. S9a. When the probe laser is off-resonant the control laser drives the  $|g_1\rangle$ - $|e_1\rangle$  transition. Decay will occur mostly towards the  $|g_1\rangle$  state and occasionally to the dark  $|g_2\rangle$  state. If the probe laser becomes resonant with the  $|g_1\rangle$ - $|e_2\rangle$  transition, the increased population in the  $|e_2\rangle$  state will prefer to decay towards the dark  $|g_2\rangle$  state. The overall decay towards the dark state is now increased. The secondary pumping scheme (Fig. S9b) works the other way around, where the diagonal transition is always driven by the control beam and a resonant probe beam will counteract some of the pumping into the dark state (now  $|g_1\rangle$ ). However, the slightly increased emission from scheme b cannot fully counteract the decreased emission from scheme a (even when  $\Omega_p = \Omega_c = \Omega'_p = \Omega'_c$ ).

## 6. MODELING OF COHERENT POPULATION TRAPPING

For fitting the CPT traces in Fig. 5 in the main text, we use a standard CPT description<sup>2</sup>, extended for strong inhomogeneous broadening of the optical transitions, and an approach similar to the one from the previous section. However (as compared to the previous section), the behavior of CPT has a more pronounced dependence on parameters, such that almost no assumptions have to be made. When taking the spin Hamiltonians as established input (section 4), the only assumption made is that the spin relaxation time in the ground state and excited state is much slower than all other decay process. This allows for setting up fitting of the CPT traces with only two free fit parameters, which correspond to the optical lifetime and the inhomogeneous dephasing time  $T_2^*$ .

Since two lasers couple both ground-state levels to a single common excited-state level, the other excited-state level will be empty. Therefore, we may describe this situation with a three-level system, where the PL is directly proportional to the excited-state population. The decay rates and Rabi frequencies are proportional to the Franck-Condon factors for spin-state overlaps  $\langle g_i|e\rangle$  in the same way as before (equations (12)-(15)). At this angle ( $\phi = 102^\circ$ ) we calculate these factors to be

$$\langle g_1|e\rangle = 0.9793 \quad (16)$$

$$\langle g_2|e\rangle = 0.2022 \quad (17)$$

according to the reasoning in section 4. We take that the  $|g_1\rangle-|e\rangle$  is a vertical transition and  $|g_2\rangle-|e\rangle$  a diagonal one.

In order to account for inhomogeneous broadening throughout the ensemble, the solution of the master equation is computed for a set of control-laser detunings  $\Delta_c$  (see Fig. S9a) around zero, its range extending far beyond the two-laser detuning values  $\delta$  (since we experimentally observed an inhomogeneous broadening much in excess of the spin splittings). In this case the probe-laser detuning becomes  $\Delta_p = \Delta_c + \delta$ . The resulting excited-state populations are integrated along the inhomogeneous broadening  $\Delta_c$  (up to the point where the signal contribution vanishes) to give the PL emission as a function of two-laser detuning  $\delta$ . Analogous to the previous section, we have to consider a secondary  $\Lambda$ -scheme in order to fully account for the inhomogeneous broadening. The total PL emission is found by adding together the excited-state populations from both schemes.

We fit this model to the data presented in Fig. 5 after subtracting a static background. We extract the inhomogeneous dephasing time  $T_2^* = 0.32 \pm 0.08 \mu\text{s}$  and an optical lifetime of  $56 \pm 8 \text{ ns}$ . The errors are estimated from the spread in extracted dephasing times and lifetimes throughout the data sets.

## 7. ANISOTROPIC $g$ -FACTOR IN THE EFFECTIVE SPIN-HAMILTONIAN

### A. Relationship between effective spin Hamiltonian and local configuration of the defect

An effective spin-Hamiltonian as the one used in the main text is a convenient tool which allows us to describe the behavior of the system in a wide range of configurations, as long as the effective parameters are experimentally determined and all relevant states are considered. It is often the meeting point between experimentalists, who measure the relevant parameters, and theoreticians, who attempt to correlate them to the Hamiltonian that describes the configuration of the system. A careful description of the latter, and how it modifies the parameters at hand, allows us to rationalize our choices when investigating defects with varying characteristics (such as a different charge state or element). This task is more approachable when we consider the group-theoretical properties of the system at hand. Here we combine group-theoretical considerations with ligand field theory in order to qualitatively describe the features observed in our experiment. In particular, we aim at explaining the large Zeeman splitting anisotropy observed in both ground and excited states, and correlating it to the charge and spatial configuration of the defect.

In our experiments, we observe a single zero-phonon line (ZPL) associated with optical transitions between two Kramers doublets (KD, doublets whose degeneracy is protected by time-reversal symmetry and is thus broken in the presence of a magnetic field) in defects which contain Mo. The presence of a single zero-phonon line in both 4H and 6H-SiC samples indicates that the defect occupies a lattice site with hexagonal symmetry. The lattice of 6H-SiC has two inequivalent sites with cubic symmetry. Thus, if the defect were to occupy sites of cubic symmetry, we would expect to observe two ZPLs closely spaced in this sample. The absence of the ZPL associated with this defect in samples of 3C-SiC<sup>3</sup> further corroborates this assumption. Additionally, we observe strong anisotropy in the Zeeman splitting of the ground and excited states. Specifically, when the magnetic field is perpendicular to the symmetry axis of the crystal, the Zeeman splitting of the ground state goes to zero, whereas that of the excited state is very small. This feature is observed in other transition-metal defects in SiC situated at Si substitutional sites of hexagonal symmetry and with one electron in its 3d orbital<sup>4</sup>, but we are not aware of a clear explanation of the phenomenon.

In our experiments, we observed transitions between sublevels of doubly degenerate ground and excited states, whose degeneracy is broken in the presence of a magnetic field. Thus, we note that ground and excited states are isolated KDs, indicating that the defect contains an odd number of electrons. A Mo atom has 6 electrons in its valence shell. The atom can occupy a Si substitutional site ( $\text{Mo}_{\text{Si}}$ ), where it needs to bond to 4 neighboring atoms, or an asymmetric split vacancy (ASV) site ( $\text{Mo}_{\text{V}_{\text{Si}}-\text{V}_{\text{C}}}$ ), where it bonds to 6 neighboring atoms. These defects can, respectively, be described by a Mo ion in the configurations  $4d^2$  and  $4d^0$ , indicating that the defect must be ionized in order to contain an odd number of electrons. Its charge state, which could be  $\pm 1$ ,  $\pm 3$ , *etc.*, is determined by the Fermi level in the crystal of interest. We note that the ZPL could only be observed in p-doped samples, which indicates that the features investigated here are unlikely to arise from negatively charged defect. The defect  $\text{Mo}_{\text{Si}}^{+1}$  (where +1 represents the charge state of the defect, not the Mo atom) can be approximately described by a Mo in a configuration  $4d^1$ , which facilitates the treatment of its configuration in terms of d orbitals. In contrast, the defect  $\text{Mo}_{\text{V}_{\text{Si}}-\text{V}_{\text{C}}}^{+1}$  is described by an electronic configuration containing a hole in the bonding orbitals. These orbitals show strong hybridization between the d orbitals of the Mo and the orbitals of the ligands, and cannot be straight-forwardly analyzed using the formalism described below. Nonetheless, inspired by the similarities between our system and other transition-metal defects reported in  $\text{SiC}^4$ , we investigate the effect of the crystal field of  $C_{3v}$  symmetry –which is expected to be significant in hexagonal lattice sites in 4H-SiC and 6H-SiC– on the one-electron levels of the 5 sublevels (10, if spin multiplicity is included) of the 4d shell of a Mo atom. We qualitatively predict the spin-hamiltonian parameters expected for a Mo ion in a  $4d^1$  configuration, and compare our analysis to the experimental results.

### **B. Ion in $4d^1$ configuration in the presence of crystal field of $C_{3v}$ symmetry and spin-orbit coupling**

The 5 degenerate sublevels of a 4d-orbital are split by a crystal field of  $C_{3v}$  symmetry<sup>5</sup>. The energy splittings induced by this field are much smaller than the energy difference between the 4d shell and the next orbital excited state (5s). This allows us to, initially, consider the 5 orbitals of the 4d shell as a complete set. Since Mo is a heavy atom, we cannot disregard the effect of spin-orbit interaction. However, we assume that the crystal field is

larger than the effect of SOC, that is,  $\Delta E_{free} \gg \Delta E_{crystal} \gg \Delta E_{spin-orbit} \gg \Delta E_{Zeeman}$ , where  $\Delta E$  denotes the energy splitting induced by each term (see Fig. S10).

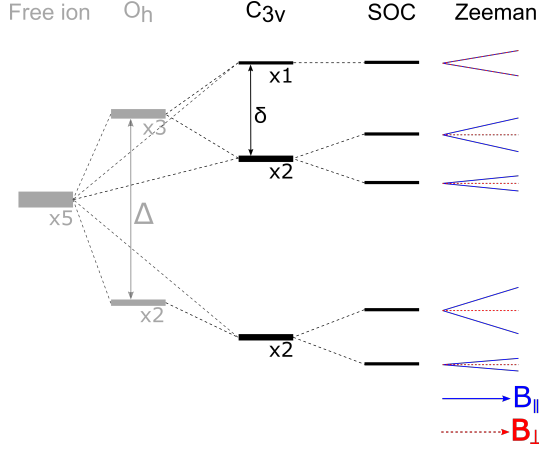


FIG. S10: **Splitting of one-electron energy levels of a 4d orbital**, under the action of a crystal field and spin-orbit coupling. In the free atom, the 5 orbitals corresponding to the 4d shell (disregarding the spin) are degenerate. A crystal field of cubic symmetry breaks this degeneracy, generating an orbital triplet and a doublet, whereas a crystal field of  $C_{3v}$  symmetry, splits the 5 orbitals into one singlet and two doublets. In the text, we focus on a crystal field of  $C_{3v}$  symmetry, and disregard the cubic term. Although we recognize that this is an approximation, we argue that this approach clarifies the physics governing the strong magnetic anisotropy observed, and is thus justified. Spin-orbit coupling is responsible for splitting the doublets, generating in total 5 sets of Kramers doublets (here, the spin of the electron is taken into account). The energy splittings caused by a magnetic field within these KD give rise to the effective spin Hamiltonian parameters considered. We note that a group-theoretical approach alone is not capable of providing the order of the energy levels shown in the figure. We take this order to be the one observed in transition-metal defects in a tetrahedral crystal field with strong trigonal distortion<sup>5</sup>.

The 5 orbital states of the d-orbital form a 5-dimensional irreducible representation (irrep) of the full rotation group  $SO(3)$ . When the symmetry is lowered by the crystal field to  $C_{3v}$ , the 5-dimensional representation is split into 2 doublets ( $E_1$ ,  $E_2$ ) and 1 singlet ( $A$ ) that are irreps of  $C_{3v}$ . Writing the 5 components of the 4d orbital in terms of the quadratic functions  $z^2$ ,  $x^2 - y^2$ ,  $xy$ ,  $xz$ ,  $yz$  allows us to identify which orbitals are degenerate in the presence of a crystal field of trigonal symmetry. We find that the singlet  $A$  is composed of the orbital  $4d_{z^2}$ . Furthermore, the orbitals  $4d_{xz}$  and  $4d_{yz}$  are degenerate upon action of

the crystal field and make up doublet  $E_1$ . Finally the orbitals  $4d_{x^2-y^2}$  and  $4d_{xy}$  correspond to doublet  $E_2$ . Group-theoretical considerations alone are not capable of elucidating which irrep corresponds to the ground state, that is, it does not provide information about the order of the energy levels.

Comparison between the Cartesian form of these 5 orbitals and the spherical harmonics which span a 5-dimensional space (that is, the spherical harmonics  $Y_l^m$  with  $l = 2$ ) allows us to rewrite the relevant orbitals as linear combinations of the eigenstates of the operators  $L^2, L_z$ . This yields a new basis for each irrep considered above:

$$E_1 : Y_2^{-2} = |d_{-2}\rangle; Y_2^2 = |d_2\rangle \quad \text{1st orbital doublet} \quad (18)$$

$$E_2 : Y_2^{-1} = |d_{-1}\rangle; Y_2^1 = |d_1\rangle \quad \text{2nd orbital doublet} \quad (19)$$

$$A : Y_2^0 = |d_0\rangle \quad \text{orbital singlet} \quad (20)$$

When the spin multiplicity is considered, each orbital doublet yields 4 possible states, whereas the orbital singlet yields 2 possible states. Spin-orbit coupling (represented by the operator  $H_{SO} = -\lambda \mathbf{L} \cdot \mathbf{S}$ ) is responsible for splitting these states into 5 different Kramers doublets:

$$\text{KD1} : |d_{+2}, +\frac{1}{2}\rangle; |d_{-2}, -\frac{1}{2}\rangle \quad (21)$$

$$\text{KD2} : |d_{+2}, -\frac{1}{2}\rangle; |d_{-2}, +\frac{1}{2}\rangle \quad (22)$$

$$\text{KD3} : |d_{+1}, +\frac{1}{2}\rangle; |d_{-1}, -\frac{1}{2}\rangle \quad (23)$$

$$\text{KD4} : |d_{+1}, -\frac{1}{2}\rangle; |d_{-1}, +\frac{1}{2}\rangle \quad (24)$$

$$\text{KD5} : |d_0, +\frac{1}{2}\rangle; |d_0, -\frac{1}{2}\rangle \quad (25)$$

where the basis vectors are given in terms of the quantum numbers  $m_l$  and  $m_s$  which denote the projection of the orbital and spin angular momentum along the quantization axis, respectively (Fig. S10). Here, the spin-orbit coupling is considered up to first order in the energy correction, whereas the wave function is corrected up to zeroth order.

A magnetic field lifts the degeneracy between the two components of each KD. This splitting is usually described phenomenologically by an effective Zeeman Hamiltonian in a system with pseudospin  $\tilde{\mathbf{S}} = \frac{1}{2}$ .

$$H_{eff} = -\mu_B \mathbf{B} \cdot \mathbf{g} \cdot \tilde{\mathbf{S}}_{1/2} \quad (26)$$

where  $\mu_B$  is the Bohr magneton,  $\mathbf{B}$  the magnetic field vector,  $\tilde{\mathbf{S}}_{1/2}$  the pseudo spin  $\frac{1}{2}$  operator and  $\mathbf{g}$  the g-tensor. In the presence of axial symmetry,  $\mathbf{g}$  can be diagonalized such that equation (26) can be rewritten in terms of the symmetry axis of the crystal

$$H_{eff} = -\mu_B \left( g_{\parallel} B_z \tilde{S}_{1/2,z} + (g_{\perp} B_x \tilde{S}_{1/2,x} + g_{\perp} B_y \tilde{S}_{1/2,y}) \right) \quad (27)$$

In terms of the eigenstates belonging to each KD, the splitting is described by the Zeeman Hamiltonian given by

$$H_{Zee} = -\mathbf{B} \cdot \boldsymbol{\mu} = -\mu_B \mathbf{B} \cdot (g_0 \mathbf{S} + k \mathbf{L}) \quad (28)$$

where  $\boldsymbol{\mu}$  is the magnetic moment operator,  $g_0$  the g-factor for a free electron,  $\mathbf{S}$  the total spin operator,  $k$  the orbital reduction factor, and  $\mathbf{L}$  the orbital angular momentum operator<sup>5,6</sup>. The orbital reduction factor  $k$ , is a factor between 0 and 1 which corrects for partial covalent bonding between the electron and the ligands<sup>5</sup> (note that the value of  $k$  differs for each of the 5 KDs in equations (21-25)). Comparison of equations (27) and (28) shows that

$$g_{\parallel} = 2 \langle g_e S_z + k L_z \rangle = \frac{2 \langle \mu_z \rangle}{\mu_B} \quad (29)$$

$$g_{\perp} = 2 \langle g_e (S_x + S_y) + k (L_x + L_y) \rangle = \frac{2 \langle \mu_x + \mu_y \rangle}{\mu_B} \quad (30)$$

As long as the magnitude of this Zeeman splitting is small compared to the spin-orbit interaction we can consider, to first order, the effect of the magnetic field in the sets formed by each KD independently. That is, we consider that the magnetic field does not mix states pertaining to two different KDs.

In order to calculate the values of  $g_{\parallel}$  and  $g_{\perp}$  for each KD defined by trigonal symmetry and spin-orbit coupling, we rewrite equation (28) as

$$H_{Zee} = -(B_z \mu_z + B_x \mu_x + B_y \mu_y) = -(B_z \mu_z + \frac{1}{2}(B_+ \mu_- + B_- \mu_+)) \quad (31)$$

where the  $+$  and  $-$  subindices denote the raising and lowering magnetic moment operators and the linear combinations  $B_x \pm i B_y$ , respectively. When we consider the basis given in equations (21-24), the matrix elements of both  $\mu_+$  and  $\mu_-$  are zero between two eigenvectors pertaining to one KD. This arises from the fact that the operator  $\mu_+$  couples states with  $(m_l, m_s)$  to states with  $(m_l + 1, m_s)$  or  $(m_l, m_s + 1)$ . Since, within a KD, there is a change in both  $m_l$  and  $m_s$  when going from one eigenvector to the other, the operators  $\mu_+$  and  $\mu_-$

cannot couple these states to each other. Explicitly, for KD1 for example, we obtain

$$\langle d_{+2}, -\frac{1}{2} | \mu_{\pm} | d_{+2}, -\frac{1}{2} \rangle = 0 \quad (32)$$

$$\langle d_{+2}, -\frac{1}{2} | \mu_{\pm} | d_{-2}, +\frac{1}{2} \rangle = 0 \quad (33)$$

$$\langle d_{-2}, +\frac{1}{2} | \mu_{\pm} | d_{-2}, +\frac{1}{2} \rangle = 0 \quad (34)$$

and in a similar way for KDs 2 through 4. Thus, up to first order, a magnetic field applied perpendicular to the crystal c-axis is not capable of lifting the degeneracies of the 4 KDs given in equations (21)-(24). Comparing these results to equation (30) we conclude that, for the 8 sublevels of the KDs 1 through 4,  $g_{\perp} = 0$ . This arises from the effect of both the crystal field of  $C_{3v}$  symmetry and SOC in decoupling and isolating KDs with the properties mentioned above. This is not the case for KD5, given in equation (25). In this case,

$$\langle d_0, -\frac{1}{2} | \mu_{\pm} | d_0, +\frac{1}{2} \rangle \neq 0 \quad (35)$$

and the degeneracy of this KD is broken in the presence of a magnetic field perpendicular to the c-axis of the crystal.

We can consider in addition the effect of spin-orbit coupling in mixing the eigenstates presented in equations (21-25). Spin-orbit coupling is responsible for mixing between the eigenstates of KD2 and KD3 (equations (22) and (23)). Since both of these KDs show  $g_{\perp} = 0$ , this mixing does not modify the expected value of  $g_{\perp}$  in neither KD. In contrast, the SOC induced mixing between KD4 and KD5 causes some deviation of  $g_{\perp}$  from 0 in KD4, since  $g_{\perp} \neq 0$  in KD5. The values of  $g_{\parallel}$  and  $g_{\perp}$  for one electron in each of the KDs described in this section are presented in table S2.

From the 5 KDs in equations (21-25), one KD is the ground state and one KD is the excited state that we address in our experiments. As said before, our group-theoretical approach cannot identify the ordering in energy of these 5 KDs. However, by looking at the g-factor properties of the KDs in table S2 we can check which ones show consistent behavior with that of the observed ground and excited state. For the observed ground state, we found  $|g_{\parallel}| < 2$  and  $g_{\perp} = 0$ . Concerning possible values for the orbital reduction factor  $k$ , by definition  $k < 1$ , and we must have  $k > 0.1$  since  $|g_{\parallel}|$  deviates substantially from 2. This suggests that KD2 is the ground state. For the excited state, we also have  $|g_{\parallel}| < 2$ , but with  $g_{\perp} \gtrsim 0$ . This suggests KD4 is the excited state we observed in our experiments. In addition, the optical transition observed is mainly polarized along the crystal c-axis of

TABLE S2: The g-factors of the Kramers doublets originated due to spin-orbit coupling within each subspace of the electronic eigenstates in a field of  $C_{3v}$  symmetry. Spin-orbit coupling is added as a perturbation, and included up to first order. The parameters  $\lambda$  and  $\delta$  are as defined in the text and in Fig. S10. Note that the g-factor values in this table can take on negative values, while in our experimental analysis we can only extract  $|g_{\parallel}|$  and  $|g_{\perp}|$ .

$C_{3v}$	Spin-Orbit	$g_{\parallel}$	$g_{\perp}$
Doublet, $m_l = \pm 2$	KD1, eq. 21	$2(2k + 1)$	0
	KD2, eq. 22	$2(2k - 1)$	0
Doublet, $m_l = \pm 1$	KD3, eq. 23	$2(k + 1)$	0
	KD4, eq. 24	$2(k - 1)$	$0 + \alpha \frac{\lambda}{\delta}$
Singlet, $m_l = 0$	KD5, eq. 25	2	$2 - \alpha \frac{\lambda}{\delta}$

the defect. Careful analysis of the selection rules associated with the double trigonal group (which includes, besides the spatial symmetry, the spin of the electron) has been reported by Kunzer *et al.*<sup>7</sup>. Comparing their results to the considerations presented in the previous paragraphs confirms that the transition between KD2 and KD4 is predominantly polarized along the crystal c-axis, as observed. Finally, we note that we could not experimentally identify secondary ZPLs corresponding to transitions between other sets of KDs, even though they are allowed by symmetry. This could be explained by a series of factors. On the one hand, some of the KDs treated could have energies above the conduction band edge in the crystal, which would impede the observation of optical transitions from and into these levels. On the other hand, the presence of these lines could be masked by the intense phonon sideband at the red side of the ZPL, or the associated photon energies fall outside our detection window.

### C. Validity of our assumptions

The model considered here is capable of qualitatively informing us about the behavior of orbitals with d character in the presence of trigonal crystal field and spin orbit coupling. It is clear that the full description of the configuration of the defect is far more subtle than

the simple model applied here. We intend to comment on this in the next paragraphs.

*a. Symmetry of the crystal field.* In our derivation, we assume that the trigonal crystal field is the prevailing term in the Hamiltonian describing the defect. This assumption is not rigorously correct, since the symmetry of defects in SiC is more accurately described by a ligand field of cubic symmetry – which determine most of its ground and excited state properties. This field is modified in the presence of axial symmetry, as is the case for defects in hexagonal lattice sites, which is generally included as a first-order perturbation term in the Hamiltonian. Nonetheless, it can be shown<sup>5,8</sup> that the large anisotropy in the Zeeman response described above, with the cancelation of  $g_{\perp}$ , is also observed in the case of a cubic field with trigonal distortion and spin-orbit coupling of similar magnitudes. The analysis, in this case, is more laborious due to the fact that mixing of the orbitals is involved, and calculating the matrix elements of the operators  $L_{\pm}$ ,  $S_{\pm}$ ,  $L_z$  and  $S_z$  is less trivial. Furthermore, this analysis would not increase our level of understanding of the system at this point, since we were only capable of observing transitions between the sublevels of two KDs in this experiment. This approach would be more profitable if transitions between other sets of KDs were observed, allowing us to unravel several parameters associated with the system, such as the strength of the spin-orbit coupling and trigonal crystal field.

*b. Charge state of the defect.* Similarly, it can be shown that the considerations presented here can be expanded to configurations where the 4d orbitals are filled by multiple electrons (for instance, a defect in a configuration  $4d^3$ ). In this case, a doubly degenerate orbital configuration (in symmetry terms, a configuration of the kind  ${}^mE$ , where  $m$  is the spin multiplicity) in the presence of a crystal field of  $C_{3v}$  symmetry gives rise to at least one KD with  $g_{\perp} = 0$  when SOC is taken into account. Nonetheless, only a negatively charged Mo in a Si substitutional site would give rise to a defect in the configuration  $4d^3$ . The absence of the ZPL in n-doped samples indicates that this is unlikely.

In addition, a similar group theoretical analysis can show that one hole in a bonding orbital of symmetry E would also give rise to  $g_{\perp} = 0$ . Thus, the features observed here could also correspond to a positively charged  $Mo_{V_{Si-V_C}}$  defect (where one of the six Mo electrons that participate in bonding is lost to the crystal lattice). Due to the strong hybridization between the Mo and the divacancy orbitals in this case, the description of this case is more subtle and will not be performed here.

## D. Summary

We showed that an analysis of the effect of the defect symmetry on the Zeeman energy splittings of its ground and excited states, combined with the experimental observations, helps us unravel the configuration of the defect studied in this work. We show that, in  $C_{3v}$  symmetry, a combination of the crystal field and spin-orbit interaction is responsible for the strong magnetic anisotropy observed experimentally. Furthermore, the fact that the defect studied in this work is only observed optically in samples which are p-doped indicates that the charge of the defect is more likely positive than negative. In this way, we conclude that the most probable configuration of our defect is a Mo ion on a Si substitutional site of  $h$  symmetry, with a charge +1, which can be approximately described by a Mo atom in a  $4d^1$  configuration. The absence of other lines associated with the defect prevents us from providing a more accurate description of the system. Nonetheless, we have developed a qualitative description based on symmetry, which explains the Zeeman splittings observed. The considerations presented here allow us to predict and rationalize the presence of strong anisotropy in other transition-metal defects in SiC. We expect neutrally charged vanadium defects in hexagonal lattice sites to show a magnetic behavior similar to the one observed in the Mo defects investigated in this work.